Exploring galaxy mass profiles in strongly lensed quasars with upcoming Roman Space Telescope observations

Esmeralda Guliqani[1*], *Lindita* Hamolli[2], and *Mimoza* Hafizi[2]

[1]Department of Mathematics and Physics, Faculty of Natural and Human Sciences, "Fan S. Noli" University of Korça, Albania
[2]Department of Physics, Faculty of Natural Sciences, University of Tirana, Albania

Abstract. Strong gravitational lensing of quasars is a powerful tool for probing cosmological parameters, tracing galaxy evolution, and investigating the internal structure of quasars. In this work, we examine the galaxy mass profiles in doubly lensed quasars expected to be detected by the Roman Space Telescope. Our previous studies suggest that, for Roman, approximately one in every 150 observed quasars will be strongly lensed by foreground galaxies, with about 85% of these events produced by a single lensing galaxy. Here, we focus on calculating the angular positions of lensed images, the time delays between them, and their magnification ratios, considering three mass density profiles: the Singular Isothermal Sphere (SIS), the Non-Singular Isothermal Sphere (NIS), and the Singular Isothermal Ellipsoid (SIE), restricted to double quasars. We simulated such systems using Monte Carlo techniques, based on observed redshift distributions of quasars and galaxies, galaxy stellar masses, and the empirical relation between stellar mass and velocity dispersion. Our results show that the SIS, NIS, and SIE models yield nearly identical predictions for angular separations, time delays, and magnification ratios. These findings suggest that future observations of doubly lensed quasars with the Roman Space Telescope may not provide clear statistical discrimination between different galaxy mass profiles, although Roman will remain a powerful instrument for collecting valuable data on gravitational lensing systems.

1 Introduction

Strong gravitational lensing is the bending of light from distant sources such as quasars by massive foreground galaxies or clusters. When the alignment between the source, lens, and observer is favorable, the quasar appears as multiple magnified images or distorted arcs. This phenomenon offers a powerful tool for probing galaxy mass distributions, exploring the internal structure of quasars, and constraining cosmological parameters.

One observable feature in lensed quasars is the time delay between their multiple images. These delays arise both from differences in the paths taken by the light and from the

* Corresponding author: eguliqani@unkorce.edu.al

gravitational potential along those paths. As proposed by Refsdal [1], time delays provide an independent method for determining the Hubble constant (H_0) [2]. In addition to the cosmic microwave background (CMB) [3] and distance-ladder methods [4], this independent method, known as Time-Delay Cosmography [1], contributes to resolving the current H_0 tension.

The mass distribution of lensing galaxies affects image positions, time delays, and magnifications. While spherical models such as the Singular Isothermal Sphere (SIS) [5] and the Non-singular Isothermal Sphere (NIS) [6] provide analytic simplicity, real galaxies often exhibit ellipticity, requiring more realistic models such as the Singular Isothermal Ellipsoid (SIE) [6, 7]. Beyond image positions and time delays, magnification ratios provide complementary constraints on the lens mass distribution. Magnification is particularly sensitive to convergence and shear at the image positions [8], and studying its correlation with image separation and configuration allows testing the accuracy of different mass models.

Understanding these lensing effects requires a large sample of lensed quasars, which upcoming surveys will provide. Currently, more than 200 lensed quasars[†] have been identified, mainly through the Sloan Digital Sky Survey (SDSS) [9] and the Cosmic Lens All-Sky Survey (CLASS) [10]. Future observatories such as the Nancy Grace Roman Space Telescope [11] and the Vera Rubin Observatory's LSST [12] are expected to greatly increase this number. Our focus is on the Roman Telescope, as it can detect smaller angular separations. The Roman Space Telescope is a NASA infrared observatory scheduled to launch in May 2027 and operate at the second Lagrange point (L2). It is equipped with the Wide Field Instrument (WFI), which includes eight filters (0.48–2.3 μm) and a coronagraph for high-contrast imaging. Roman will survey about 2,000 deg² over five years, with an imaging cadence of 5 days and an angular resolution of ~0.1″ [13]. In our previous work [5], we estimated the number of quasars that the Roman Telescope is expected to detect with the F213 filter (wavelength range 1.95–2.30 μm) of the WFI, considering four different survey modes. We found that the number of detectable quasars depends strongly on the limiting magnitudes, higher limiting magnitudes correspond to a larger number of observable quasars. Another important capability of Roman is its high angular resolution, which will increase the probability of identifying quasars that will be lensed by foreground galaxies. Meanwhile, the ground-based LSST telescope [12] has a lower angular resolution (0.7″), making it impossible to resolve lensed images that are very close to each other. However, LSST has a wide-area survey, which, when combined with Roman, will provide large statistical samples of lensed quasars, enabling more robust studies of lensing effects.

In this work, we examine how three lens mass models: SIS, NIS, and SIE, affect the image positions, time delays, and magnification ratios of lensed quasars observable with the Roman Telescope. Our analysis focuses exclusively on double quasars. The structure of the paper is as follows: Section 2 reviews the fundamentals of strong gravitational lensing and the calculation of time delays and magnification for double images in the SIS, NIS, and SIE models. Section 3 describes our simulations and presents the results, while Section 4 provides a summary of our findings.

2 Strong gravitational lensing

Strong gravitational lensing is the bending of light from a distant object (such as a quasar or galaxy) due to the gravitational field of a massive object (like a galaxy or cluster) located

[†] https://research.ast.cam.ac.uk/lensedquasars/doubles.html

between the source and the observer. This effect can produce magnified, distorted, or even multiple images of the background source.

Given the source position and the lens potential in a gravitational lens system, the image positions can be determined by solving the lens equation [6, 7]. This relation in dimensionless form is:

$$\mathbf{y} = \mathbf{x}_i - \boldsymbol{\alpha}(\mathbf{x}_i), \quad \text{i = 1 or 2} \tag{1}$$

where $\mathbf{y}$ is the dimensionless position of the source, $\mathbf{x}_i$ is the dimensionless position of the i-th image, and $\boldsymbol{\alpha}(\mathbf{x}_i)$ is the scaled deflection angle due to the lensing mass. The gravitational deflection angle at a position $\mathbf{x}_i$ is defined as the gradient of the gravitational potential $\Psi(\mathbf{x}_i)$: $\boldsymbol{\alpha}(\mathbf{x}_i) = \nabla \Psi(\mathbf{x}_i)$. When the source, lens, and observer are perfectly aligned, the light from the source is deflected symmetrically around the lens, resulting in a circular image known as the Einstein ring. The Einstein radius ξ_0 defines the radius of this ring:

$$\xi_0 = \sqrt{\frac{4GM}{c^2}\frac{D_{LS}D_L}{D_S}} \tag{2}$$

where G is the gravitational constant, M is the mass of the lensing galaxy, c is the speed of light in vacuum, D_S, D_L, dhe D_{LS} are the observer-source, observer-lens, and lens-source angular diameter distances, respectively. The Einstein radius ξ_0 is related to the Einstein angle θ_0 by the relation $\theta_0 = \xi_0 / D_L$. If the surface mass density of the lens $\Sigma \geq \Sigma_{crit}$, where:

$$\Sigma_{crit} = \frac{c^2}{4\pi G}\frac{D_S}{D_{LS}D_L} \tag{3}$$

is the critical surface density, multiple images are formed. This means that the convergence $\kappa = \Sigma / \Sigma_{crit}$ exceeds unity (i.e., $\kappa \geq 1$).

When multiple images of a background source are formed due to lensing, the light does not arrive at the same time. The time delay Δt for an image at the position $\mathbf{x}_i$ relative to the unlensed light path is given by:

$$\Delta t(\mathbf{x}_i) = \frac{1+z_L}{c}\frac{D_S \xi_0^2}{D_L D_{LS}}\left[\frac{1}{2}(\mathbf{x}_i - \mathbf{y})^2 - \Psi(\mathbf{x}_i)\right] + \text{const} \tag{4}$$

where z_L is the redshift of the lens. Since the unlensed source is not observable, the time delay Δt can not be measured. But, if the variable source is strongly lensed, an observable quantity is the relative time delays between images, which for two images, i and j, can be written as:

$$\Delta t_{i,j} = \frac{1+z_L}{c}\frac{D_S \xi_0^2}{D_L D_{LS}}\left[\frac{1}{2}(\mathbf{x}_i - \mathbf{y})^2 - \frac{1}{2}(\mathbf{x}_j - \mathbf{y})^2 - \Psi(\mathbf{x}_i) + \Psi(\mathbf{x}_j)\right] \tag{5}$$

The linearized mapping from the image plane to the source plane is described by the Jacobian matrix A, which is the first-order derivative of the lens equation in a two-dimensional space:

$$A = \frac{\delta \mathbf{y}}{\delta \mathbf{x}} = \begin{pmatrix} 1-\kappa-\gamma_1 & -\gamma_2 \\ -\gamma_2 & 1-\kappa+\gamma_1 \end{pmatrix} \tag{6}$$

where γ_1 and γ_2, expressed as second-order derivatives of Ψ, are the components of the shear $\gamma^2 = \gamma_1^2 + \gamma_2^2$ [6, 7]. The shear γ quantifies the stretching and distortion of images without changing their brightness. Both convergence and shear determine the magnification of the i-th image:

$$\mu(\mathbf{x}_i) = \left(\det \frac{\partial \mathbf{y}}{\partial \mathbf{x}_i} \right)^{-1} = \frac{1}{(1-\kappa)^2 - \gamma^2} \tag{7}$$

The sign of magnification is referred to as parity. Multiple images form when the lens system has sufficient surface mass density and the total magnification diverges, which occurs near the critical curves where $(1 - \kappa)^2 - \gamma^2 = 0$. This condition defines the critical curves in the image plane, while the corresponding points in the source plane are known as caustics. Below, we present all the quantities described above for the SIS, NIS, and SIE models.

2.1 Singular isothermal sphere (SIS) lens model

One of the simplest models of the strong lensing from galaxies and galaxy clusters is the Singular Isothermal Sphere (SIS) [5-7]. This model describes a spherical mass distribution with surface mass density $\Sigma(\xi) = \sigma^2 / 2G\xi$, where σ is a one-dimensional velocity dispersion and ξ is the distance from the lens center on the lens plane [14]. The Einstein radius for this model is given as $\xi_0 = 4\pi\sigma^2 D_{LS} D_L / c^2 D_S$. If the source lies within the Einstein ring ($y < 1$), the lens equation yields two solutions. These correspond to two images positioned on opposite sides of the source, one inside the Einstein ring ($x_2 = y - 1$) and the other outside it ($x_1 = y + 1$), with the source aligned along a straight line. A schematic representation of this configuration is shown in Fig. 1.

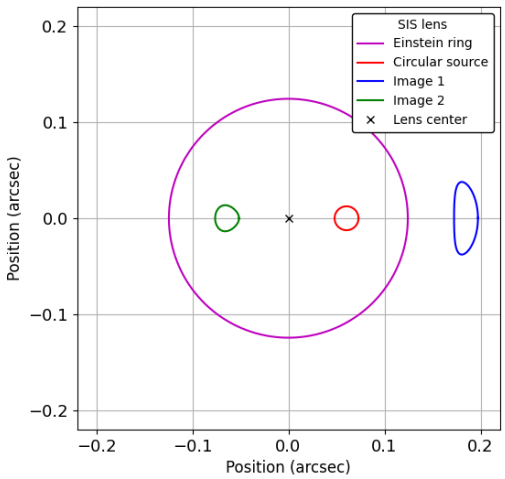

Fig. 1. Positions of the lens, source, images, and Einstein ring for the SIS lens model. The source is assumed to be circular, with a radius of 1.2E-2 arcsec.

The separation between the two images, expressed in units of the Einstein radius, is Δx = 2. The time delay between two lensed images when the lens is assumed to be described by the SIS model is $\Delta t_{12} = \frac{1+z_L}{c^2}\frac{\xi_0^2 D_S}{D_L D_{LS}}\left(x_1^2 - x_2^2\right)$. The convergence and the shear for the SIS model are $\kappa(x) = \gamma(x) = 1/(2x)$. We calculate the magnification of a lensed image in the SIS model as a function of convergence and shear, as given by $\mu = |x|/(|x|-1)$. As a result, the image located at x_1 is magnified with positive parity, while the image at x_2 has negative parity and may be either magnified or demagnified. While the SIS model has known limitations, such as a central singularity and infinite total mass, it still serves as a useful representation for galactic lenses. A more realistic approach is to introduce a core radius at the center.

2.2 Non-singular isothermal sphere (NIS) lens model

The Non-singular Isothermal Sphere lens model is the case when the lens has a finite-density core with radius ξ_c [6, 7]. For this model, the surface mass density is given by $\Sigma(\xi) = \sigma^2/\left(2G\sqrt{\xi^2+\xi_c^2}\right)$ [6, 7]. The Einstein ring for the NIS lens model has a radius $\xi_{ENIS} = \xi_0\sqrt{1-(2\xi_c/\xi_0)}$, where ξ_0 is the Einstein radius for the SIS model. This ring represents the critical line of the source located at y = 0. There is another critical line with a radius $x_r = \sqrt{x_c}\left[1-\frac{x_c}{2}\left(1+\sqrt{1+\frac{4}{x_c}}\right)\right]^{1/2}$ smaller than the Einstein radius [15]. The corresponding caustic line is a circle with radius $y_r = y(x_r)$. When $x_c < 1/2$, and the source is inside the caustic, $y < y_r$ the lens equation has three real solutions. Two images lie within the Einstein ring, while one lies outside it (Fig. 2).

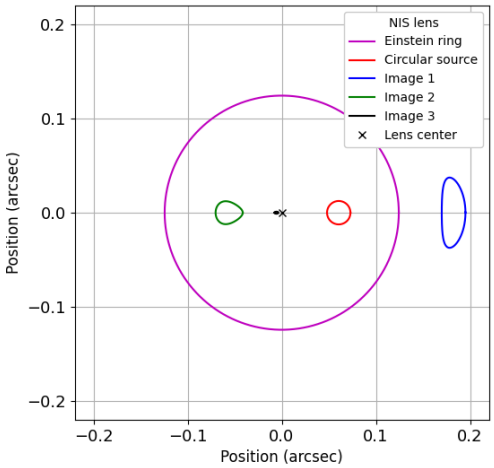

Fig. 2. The positions of the lens, source, images, and Einstein ring for the NIS lens model. The circular source has a radius of 1.2E-2 arcsec, and the core radius of the lens is 3.4E-3 arcsec.

Since the central image is generally difficult to detect because it is demagnified and lies close to the lens galaxy, we consider only two external images. The gravitational potential for the NIS model given by:

$$\Psi(x)=\left[\sqrt{x^2+x_c^2}-x_c\ln\frac{\xi_0}{D_L}\left(\sqrt{x^2+x_c^2}+x_c\right)\right], \tag{8}$$

is used to find the time delay between images, as shown in equation (5). By applying the convergence $\kappa(x)=1\Big/\left(2\sqrt{x^2+x_c^2}\right)$ and shear:

$$\gamma(x)=\left[\left(\frac{\sqrt{x^2+x_c^2}-x_c}{x^2}\right)-\frac{1}{2\sqrt{x^2+x_c^2}}\right] \tag{9}$$

to equation (7), we derive the magnification for each image of the NIS model. The first image, located outside the Einstein ring, is magnified and has positive parity, while the second image, positioned inside the Einstein ring but farther from the lens center, has negative parity and may be either magnified or demagnified.

2.3 Singular isothermal ellipsoid (SIE) lens model

The Singular Isothermal Ellipsoid (SIE) model can be derived from the Singular Isothermal Sphere (SIS) model. By substituting $\xi=\sqrt{\xi_1^2+f^2\xi_2^2}\Big/\sqrt{f}$ into the surface mass density of the SIS model, the surface mass density of a singular isothermal ellipsoid galaxy becomes $\Sigma(\xi)=\sigma^2\sqrt{f}\Big/\left(2G\sqrt{\xi_1^2+f^2\xi_2^2}\right)$. Here, ξ_1 and ξ_2 are two axes in the plane of the lens, and f is the ratio of the semi-minor to semi-major axis of the ellipse, $0<f\le 1$ [6, 7]. The semi-major axis of the ellipse (galaxy) is along ξ_2. In this case, for simplicity, all relevant quantities such as convergence, lensing potential, and shear are represented in polar coordinates (x, φ) [6, 7]. The convergence for this model in polar coordinates is given as:

$$\kappa(x,\varphi)=\frac{\sqrt{f}}{2x\sqrt{\cos^2\varphi+f^2\sin^2\varphi}} \tag{10}$$

The solution of the Poisson equation $\nabla^2\Psi=2\kappa$, is the potential:

$$\Psi(x,\varphi)=x\frac{\sqrt{f}}{f'}\left[\sin\varphi\arcsin\left(f'\sin\varphi\right)+\cos\varphi\arcsin h\left(\frac{f'}{f}\cos\varphi\right)\right] \tag{11}$$

From this potential, two components of shear can be found by:

$$\begin{aligned}\gamma_1(x)&=-\kappa(x)\cos 2\varphi\\ \gamma_2(x)&=-\kappa(x)\sin 2\varphi\end{aligned} \tag{12}$$

and $\gamma = \sqrt{\gamma_1^2 + \gamma_2^2} = \kappa$ [6]. These values are used to calculate the magnification through equation (7). By applying Brent's method [16] in Python, the angular positions of the images are determined as solutions of the lens equation. Depending on the source position, on-axis ratio f, and the orientation of the galaxy, the lens equation for this model may yield one, two, three, or four images. When the source lies inside the cut [6, 7] but outside the caustic, two images are formed, as illustrated schematically in Fig. 3. The first image is magnified, has positive parity, and appears outside the critical curve in the lens plane. In contrast, the second image is demagnified, has negative parity, and forms close to the lens center, within the critical curve. The time delay between the lens images is calculated using equation (5).

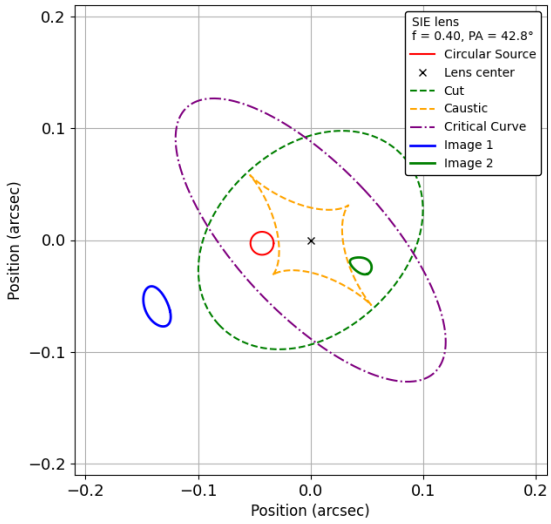

Fig. 3. The positions of the lens, source, images, critical line, cut, and caustic for double systems of the SIE lens model. The source is assumed to be circular, with a radius of E-2 arcsec.

3 Simulations and results

To investigate lens models in doubly lensed quasars with the Roman Space Telescope, we employed a Monte Carlo approach. The simulations were designed to generate galaxy–quasar pair parameters based on observed redshift distributions of quasars and galaxies, the stellar mass of lensing galaxies, and the empirical relation between stellar mass and velocity dispersion. Specifically, we generated:

- *Quasar redshifts* using data from the MILLIQUAS (Millions of Quasars) catalog [17], which contains 1,021,800 observed quasars.
- *Galaxy redshifts* from the distribution obtained by Appenzeller et al. [18], with the restriction that the galaxy redshift must be smaller than that of the corresponding quasar. For each quasar, the number of galaxies satisfying this condition was determined from the cumulative galaxy distribution.
- *Galaxy stellar masses* using the relation from Davidzon et al. [19]. Based on the COSMOS2015 catalog, the authors provided a comprehensive view of stellar mass assembly

across the redshift range $z = 0.1$ to $z = 6$. The measurements were fitted with a double Schechter function up to $z = 3$, and with a single Schechter function beyond that limit.

- *Stellar velocity dispersions* derived from the relation proposed by Zahid et al. [20]. By analyzing SDSS and SHELS survey data, the authors established a correlation between central stellar velocity dispersion and stellar mass.

Assuming a flat universe with cosmological parameters: $\Omega_m = 0.30$, $\Omega_k = 0$, $\Omega_\lambda = 0.70$ and $H_0 = 70 kms^{-1}Mpc^{-1}$, we calculated the angular diameter distances from the redshifts following Liao [21].

For each quasar–galaxy pair, we computed the Einstein angle by $\theta_0 = 4\pi \frac{\sigma^2}{c^2} \frac{D_{LS}}{D_S}$ in radians, since the measured central stellar velocity dispersion of the lens galaxy reflects the total mass enclosed within the Einstein radius, and provides a velocity scale consistent with that derived from the singular isothermal sphere model [22]. The probability that a galaxy lies within the Einstein angle along the quasar–galaxy line of sight is given by $10^8 \theta_0^2 / 14$, normalized to the total number of galaxies, estimated at 200 billion across the sky [23]. Each system was accepted as a lensing event if a uniformly drawn random number in the interval (0, 1) was smaller than the estimated lensing probability; otherwise, it was rejected. This procedure was applied to the entire quasar sample.

We simulated a population of 100,000 strong lensing events. By applying an angular resolution limit of 0.1 arcseconds, corresponding to the expected performance of the Roman Space Telescope, we identified 578 quasars lensed by a single galaxy, with Einstein angular radius above the detection threshold. For each lensing galaxy, we employ three models: SIS, NIS, and the SIE model, and since for the last model we needed the axis ratio *f* and position angle (PA) we extracted them from the HyperLeda catalog[‡], where the position angle defines the orientation of the galaxy's major axis measured from North ($PA = 0$ corresponds to a North–South alignment).

Since the SIE model can produce two, three, or four images, our analysis focuses only on double quasars. From the entire sample, we selected and used for further calculations only those systems with two images. After applying these criteria, the final sample consists of 473 double quasars. For this sample, we calculated the image positions, angular separations, time delays, and magnification ratios. Fig. 4 shows the redshift distribution of the quasars and their lensing galaxies in the final sample. As shown, the redshifts of the quasars z_S range from about 0.5 to over 5, with a peak around $z_S \approx 1.8$, while the lensing redshifts of galaxies z_L are primarily located at lower redshifts, ranging from 0.1 to 2.1, and peaking around $z_L \approx 0.5$.

For the three lens models, we calculated the image positions and determined the angular separations between the double images. The results are presented in Fig. 5, which shows the probability distribution of image separations in arcseconds, plotted on a logarithmic scale with a bin width of 0.05. The angular separations of double images range from 0.2–9.7 arcsec in the SIS model, 0.17–9.57 arcsec in the NIS model, and 0.17–9.51 arcsec in the SIE model. The distributions indicate that the three models predict nearly identical angular separations, with a slight tendency toward smaller values in the SIE and NIS cases. For the NIS model, this behavior is expected since the images tend to be closer together. In the case of the SIE model, the angular separation depends on the axis ratio, the orientation angle, and the position of the source relative to the caustics.

[‡] http://atlas.obs-hp.fr/hyperleda/a106/

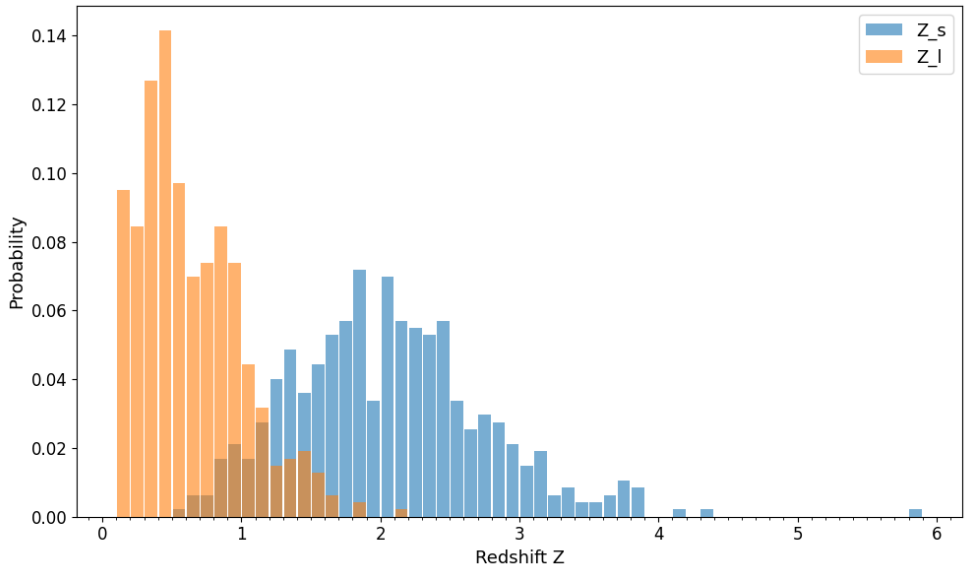

Fig. 4. Probability distribution of the redshift for quasars and galaxies. The blue bars represent the distribution of quasars, and the orange bars represent the distribution of galaxies. The width of each bar is 0.1.

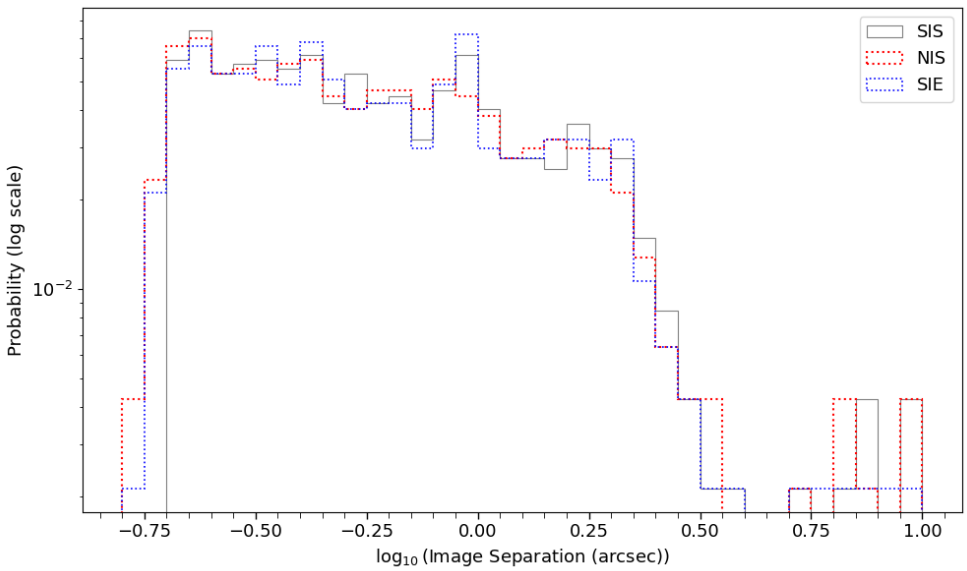

Fig. 5. Probability distribution of image separations (in arcseconds) on a logarithmic scale for double quasars expected to be observed by the Roman Space Telescope. The gray line represents the SIS model, the red dotted line the NIS model, and the blue dotted line the SIE model. Bin width on the logarithmic scale is 5E-2.

In addition to image separations, we calculated the time delays between lensed images using three models: SIS, NIS, and SIE. In the SIS model, time delays range from 5.04 hours to 5 years, with a median of 11.5 days. For the NIS model, the time delays span from 4.6 hours to 5 years, with a median of 11.29 days. The SIE model produces time delays between 5.5 hours and 5.3 years, with a median of 11.75 days. The resulting time-delay distributions (in days), shown on a logarithmic scale in Fig. 6 with a bin width of 0.1, indicate that all three lens models yield comparable ranges, extending from a few hours to several years. This result is consistent with the findings of [24], who demonstrated that isothermal models yield comparable time delays, with differences arising primarily from image positions rather than from ellipticity. It also agrees with [25], who emphasized that the radial mass profile has the strongest influence on time delays, while the angular structure of the potential plays a secondary role.

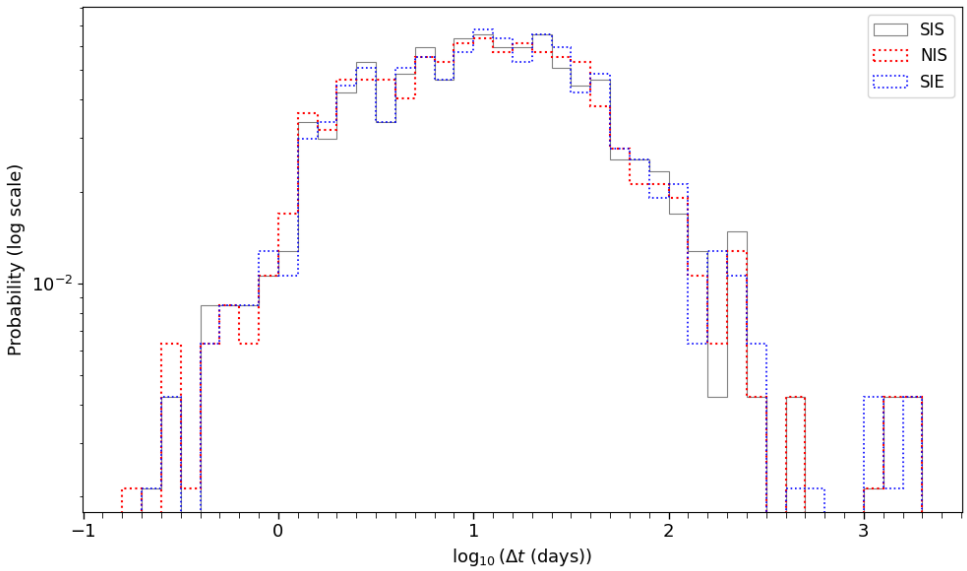

Fig. 6. Probability distribution of time delays (in days) on a logarithmic scale for double quasars expected to be observed by the Roman Space Telescope. The gray line represents the SIS model, the red dotted line the NIS model, and the blue dotted line the SIE model. Bin width on the logarithmic scale is 0.1.

The last quantity we examined is the magnification ratio between the two images of each quasar–galaxy system. It is defined as the ratio of the magnification of the image with the larger absolute value to that of the other image for each lens profile. Fig. 7 shows the probability distributions of these magnification ratios on a logarithmic scale, with a bin width of 0.1. In the SIS model, the ratios range from 1.1 to about 244, with a median of 5.4. In the NIS model, they vary between 0.7 and about 239, with a median of 4.8. The SIE model produces ratios from 1 up to about 336, with a median of 5.5. Overall, the magnification ratios cover a wide range, from values near unity to several hundred. However, the median values are very similar across all three models, indicating that they produce comparable magnification effects.

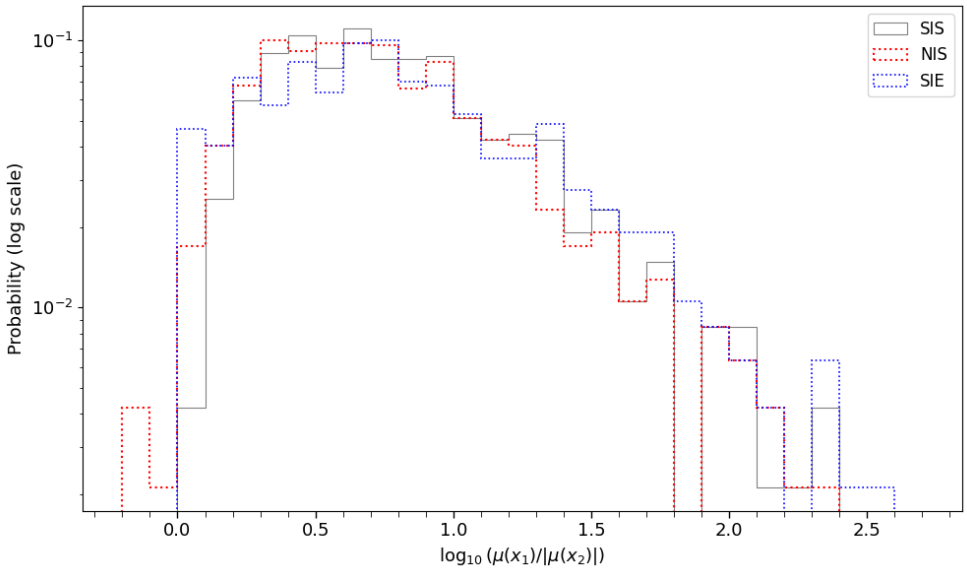

Fig. 7. Probability distribution of the magnification ratios on a logarithmic scale for double quasars expected to be observed by the Roman Space Telescope. The gray line represents the SIS model, the red dotted line the NIS model, and the blue dotted line the SIE model. Bin width on the logarithmic scale is 0.1.

4 Conclusion

We studied how the Roman Space Telescope can probe the mass profiles of lensing galaxies using a simulated sample of doubly lensed quasars. To do this, we ran Monte Carlo simulations of 100,000 strong lensing events. An event was considered observable if its Einstein angular radius was larger than the telescope's resolution of 0.1 arcsec. From these, we selected 473 double-lensed quasars and modeled them with three galaxy lens profiles: SIS, NIS, and SIE. The results show that the angular separations predicted by the models are nearly identical, with slightly smaller values in the SIE and NIS cases. The time delays between lensed images are also consistent across the three models, with median values of about 11 days and ranges spanning from a few hours to several years. Moreover, the magnification ratios are similarly comparable across the models.

In this study, the effect of dust in lens galaxies was not considered. Dust absorbs and scatters light, making lensed images appear fainter or redder, but it does not alter their angular positions or gravitational time delays [26]. Depending on its distribution, dust can distort the observed light profile of the lens galaxy, potentially introducing biases in inferred axis ratios or position angles in the SIE model. Such biases may affect the interpretation of lensing geometry and the derived parameters. These effects will be addressed in a forthcoming paper.

In conclusion, these findings for doubly lensed quasars suggest that future observations with the Roman Space Telescope may not provide clear statistical insights for distinguishing between the mass profiles of lensing galaxies. This is because, across the three models considered, the observable quantities exhibit nearly identical distributions, with only a slight shift toward smaller values in the angular separation of the images. These results highlight that, although the Roman Space Telescope has strong potential to collect valuable data on gravitational lensing systems, its ability to discriminate between different galaxy mass profile models remains limited in this analysis.

We gratefully acknowledge the financial support from “Fan S. Noli” University, University of Korça, which made this research possible.
All the results presented in this paper are derived from rigorous numerical calculations based on the equations provided in the paper. No new data was created.
The contribution of the authors to this work is as follows: conceptualization, E. G., L. H., and M. H.; methodology, E. G., L. H., and M. H.; software, E. G., and L. H.; validation, E. G., L. H., and M. H.; writing - original draft preparation, E. G.; writing – review and editing, E. G., L. H., and M. H.; supervision, L. H., and M. H.

References

1. S. Refsdal, On the Possibility of Determining Hubble’s Parameter and the Masses of Galaxies from the Gravitational Lens Effect. Mon. Not. R. Astron. Soc. **128**, 307 (1964). https://doi.org/10.1093/mnras/128.4.307
2. P. Schechter, The Hubble constant from gravitational lens time delays. Proc. Int. Astron. Union. 281 (2004).
3. N. Aghanim, Y. Akrami, M. Ashdown, J. Aumont, C. Baccigalupi, M. Ballardini, A.J. Banday, R.B. Barreiro, N. Bartolo, S. Basak, R.A. Battye, K. Benabed, J. Bernard, M. Bersanelli, P. Bielewicz, J.J. Bock, J.R. Bond, J. Borrill, F.R. Bouchet, … A. Zonca, Planck 2018 results. Astron. Astrophys. **641**, A6 (2020). https://doi.org/10.1051/0004-6361/201833910
4. A.G. Riess, S. Casertano, W. Yuan, J.B. Bowers, L.M. Macri, J. Zinn, D. Scolnic, Cosmic Distances Calibrated to 1% Precision with Gaia EDR3 Parallaxes and Hubble Space Telescope Photometry of 75 Milky Way Cepheids Confirm Tension with ΛCDM. Astrophys. J. **908**, L6 (2021). https://doi.org/10.3847/2041-8213/abdbaf
5. L. Hamolli, M. Hafizi, F. De Paolis, E. Guliqani, Investigating Gravitationally Lensed Quasars Observable by Nancy Grace Roman Telescope. Galaxies. **1**, 0 (2023a). https://doi.org/10.3390/galaxies11030071
6. M. Meneghetti, Introduction to Gravitational Lensing With Python Examples, Lecture notes in Physics, (Springer, 2021).
7. R. Kormann, P. Schneider, and M. Bartelmann, Isothermal elliptical gravitational lens models. Astron. Astrophys. **284**, 285 (1994).
8. E. Guliqani, L. Hamolli, M. Hafizi, Predicting the Gravitational Lensing Magnification of Quasars by the Roman Space Telescope. Turk. J. Phys. **49**, 169 (2025). https://doi.org/10.55730/1300-0101.2783
9. D.G. York, J. Adelman, J.E. Anderson, S. F. Anderson, J. Annis, N.A. Bahcall, J.A. Bakken, R.H. Barkhouser, S. Bastian, E. Berman, W.N. Boroski, S. Bracker, C. Briegel, J.W. Briggs, J. Brinkmann, R. Brunner, S. Burles, L.N. Carey, M. Carr, …. A.G. Pauls, The Sloan Digital Sky Survey: Technical Summary. Astron. J. **120**, 1579 (2000). https://doi.org/10.1086/301513
10. S. Myers, N. Jackson, I.W.A. Browne, A.G. De Bruyn, T.J. Pearson, A.C.S. Readhead, P.N. Wilkinson, A.D. Biggs, R.D. Blandford, C.D. Fassnacht, L.V.E. Koopmans, D.R. Marlow, J.P. McKean, M. Norbury, P. Phillips, D. Rusin, M.C. Shepherd, C.M. Sykes, The Cosmic Lens All-Sky Survey - I. Source selection and observations. Mon. Not. R. Astron. Soc. **341**, 1 (2003). https://doi.org/10.1046/j.1365-8711.2003.06256.x
11. D. Spergel, N. Gehrels, C. Baltay, D. Bennett, J. Breckinridge, M. Donahue, A. Dressler, B.S. Gaudi, T. Greene, O. Guyon, C. Hirata, J. Kalirai, N.J. Kasdin, B. Macintosh, W. Moos, S. Perlmutter, M. Postman, B. Rauscher, J. Rhodes, Y. Wang, D.

Weinberg, D. Benford, M. Hudson, W.S. Jeong, Y. Mellier, W. Traub, T. Yamada, P. Capak, J. Colbert, D. Masters, M. Penny, D. Savransky, D. Stern, N. Zimmerman, R. Barry, L. Bartusek, K. Carpenter, E. Cheng, D. Content, F. Dekens, R. Demers, K. Grady, C. Jackson, G. Kuan, J. Kruk, M. Melton, B. Nemati, B. Parvin, I. Poberezhskiy, C. Peddie, J. Ruffa, J.K. Wallace, A. Whipple, E. Wollack, F. Zhao, Wide-Field InfrarRed Survey Telescope-Astrophysics Focused Telescope Assets WFIRST-AFTA 2015 Report. Instrum. Methods Astrophys. 1 (2015). https://arxiv.org/abs/1503.03757.

12. M. Oguri, P.J. Marshall, Gravitationally lensed quasars and supernovae in future wide-field optical imaging surveys. Mon. Not. R. Astron. Soc. **405**, 2579 (2010). https://doi.org/10.1111/j.1365-2966.2010.16639.x
13. R. Beaton, H. Al-Kowski, A. Bellini, S. Casertano, C. Christian, R. Cosentino, G. De-Rosa, et al. The Roman Space Telescope Science Operations Center: News and updates. Astrophys. J. **55**, (2023).
14. A. Eigenbrod, Gravitational Lensing of Quasars, (EPFL Press, 2011).
15. S. Mollerach, E. Roulet, Gravitational lensing and microlensing, (World Scientific, 2002).
16. R.P. Brent, Algorithms for minimization without derivatives. Comput. J. **14**, 4 (1971).
17. E.W. Flesch, The Million Quasars (Milliquas) Catalogue, v6.4. astro-ph.GA. (2019). https://arxiv.org/abs/1912.05614v1
18. I. Appenzeller, R. Bender, A. Böhm, F. Stephan, K.J. Fricke, A. Gabasch, J. Heidt, U. Hopp, K. Jäger, D. Mehlert, S. Noll, R. Saglia, S. Seitz, C. Tapken, B. Ziegler, Exploring Cosmic Evolution with the FORS Deep Field. Messenger. **116**, 18 (2004). http://pubman.mpdl.mpg.de/pubman/item/escidoc:949258
19. I. Davidzon, O. Ilbert, C. Laigle, J. Coupon, H.J. McCracken, I. Delvecchio, D. Masters, P. Capak, B.C. Hsieh, O. Le Fèvre, L. Tresse, M. Bethermin, Y.Y. Chang, A.L. Faisst, E. Le Floc'h, C. Steinhardt, S. Toft, H. Aussel, C. Dubois, G. Hasinger, M. Salvato, D.B. Sanders, N. Scoville, J.D. Silverman, The COSMOS2015 galaxy stellar mass function. Thirteen billion years of stellar mass assembly in ten snapshots. Astron. Astrophys. **605**, A70 (2017). https://doi.org/10.1051/0004-6361/201730419
20. H.J. Zahid, M.J. Geller, D.G. Fabricant, H.S. Hwang, THE SCALING OF STELLAR MASS AND CENTRAL STELLAR VELOCITY DISPERSION FOR QUIESCENT GALAXIES ATz< 0.7. Astrophys. J. **832**, 203 (2016). https://doi.org/10.3847/0004-637x/832/2/203
21. K. Liao, Measuring the Distances to Quasars at High Redshifts with Strong Lensing. Astrophys. J. **883**, 3 (2019). https://doi.org/10.3847/1538-4357/ab39e6
22. A. Bolton, T. Treu, L. V. E. Koopmans, R. Gavazzi, L. A. Moustakas, S. Burles, D. J. Schlegel, R. B. Wayth, The Sloan Lens ACS Survey. VII. Elliptical Galaxy Scaling Laws from Direct Observational Mass Measurements. Astrophys. J. **684**, 248 (2008). https://doi.org/10.1086/589989
23. S. Beckwith, M. Stiavelli, A.M. Koekemoer, J.A.R. Caldwell, H.C. Ferguson, R.N. Hook, R.A. Lucas, L. Bergeron, M.R. Corbin, S. Jogee, N. Panagia, M. Robberto, P. Royle, R.S. Somerville, M. Sosey, The Hubble Ultra Deep field. Astron. J. **132**, 1729 (2006). https://doi.org/10.1086/507302
24. H. J. Witt, S. Mao & C. R. Keeton, Analytic Time Delays and H_0 Estimates for Gravitational Lenses. Astrophys. J. **544**, 98 (2000). https://doi.org/10.1086/317201

25. M. Oguri, Gravitational Lens Time Delays: A Statistical Assessment of Lens Model Dependences and Implications for the Global Hubble Constant. Astrophys. J. **660**, 1 (2007). https://doi.org/10.1086/513093
26. R. Perna, A. Loeb & M. Bartelmann, Effects of Dust on Gravitational Lensing by Spiral Galaxies. Astrophys. J. **488**, 550 (1997). https://arxiv.org/abs/astro-ph/9705172